Exploration of 3D printing technologies for the development of an affordable fluorescence detector for capillary separations

A Thesis Presented for the

Master of Science

Degree

The University of Tennessee, Knoxville

Kevin Do

December 2019

© by Kevin Do, 2019
All Rights Reserved.

This work is dedicated to my family and close friends who have helped me get to where I am today. I could not be more grateful to all of you. Thanks for keeping me sane in this journey.

Abstract

Capillary separation techniques offer fast separation for solutions of low detection volumes on the order of nL within seconds to minutes. However, detection efficiency is generally reliant on high cost commercialized instrumentation. 3D printing is a relatively new and exciting field that has opened in the world of spectroscopic methods. The ability to quickly fabricate devices have dramatically closed the gap between design and prototyping phases of a project.

In chapter 2, 3D printing technology will be used to design, develop, and optimize a fluorescence detector that can be used as an alternative to commercial instruments. This design will follow exploration of integrated optics to further improve limits of detection (LOD). The detector offers a variety of applications including biological studies. Chapter 3 will describe the detector's use for fluorescence polarization measurements along with future directions to improve the design.

Table of Contents

1 Introduction **1**

1.1 Motivation . . . 1

1.2 Capillary electrophoresis . . . 2

1.3 Fourier transform electrophoresis . . . 3

1.3.1 CE immunoassay . . . 4

1.3.2 Multispectral fluorescence detection mode . . . 5

1.3.3 Fluorescence polarization . . . 6

1.4 Frequency modulation . . . 7

1.5 3D printing . . . 8

2 Development of a miniaturized fluorescence detector for CE **10**

2.1 Introduction . . . 10

2.2 Material and methods . . . 14

2.2.1 Reagents . . . 14

2.2.2 Device fabrication and assembly . . . 14

2.2.3 Calibration curve development . . . 17

2.2.4 LED frequency modulation . . . 18

2.3 Results and discussion . . . 18

2.3.1 Ball lens alignment . . . 18

2.3.2 Confocal lens system . . . 18

2.3.3 Linear polarization filter characterization . . . 21

2.3.4 Improved fluorescence collection by reflection . . . 27

2.3.5 Digital frequency modulation . . . 27

2.4 Conclusion 28

3 3D Printed detectors for fluorescence polarization measurements 31

3.1 Introduction 31

3.2 Material and methods 32

3.2.1 Reagents 32

3.2.2 Experimental setup 32

3.2.3 Polarization calculations 32

3.3 Results and discussion 33

3.3.1 Detection performance 33

3.3.2 pH dependence 33

3.3.3 Polarization experiments 35

3.4 Future directions 35

3.4.1 Reflection grating 36

3.4.2 Future designs 37

3.5 Conclusion 41

Bibliography 42

Appendices 47

A Additional schematics 48

Vita 50

List of Tables

2.1 LOD of different dual polarizer systems 22

3.1 pH dependence of quantum yield of fluorescein 33

List of Figures

1.1 Capillary electrophoresis mechanism diagram 9

2.1 Previous iteration of miniaturized detector 12
2.2 Single vs. dual lens alignment 15
2.3 Increased fluorescence collection by reflection diagram 16
2.4 Polarizer filter placement 17
2.5 LOD vs. ball lens alignment 19
2.6 Optimization of LED current plot in single and dual lens systems 20
2.7 LOD comparison between single and dual lens systems 23
2.8 Pinhole structural integrity 24
2.9 Scatter vs. polarizer orientations 25
2.10 LOD of optimized detector with $\parallel$+$\perp$ polarizers 26
2.11 LOD of optimized detector with both polarizers and refelctor 29
2.12 Signal-noise ratio of frequency modulated excitation 30

3.1 Noise dependence of LOD in $\parallel$ and $\perp$ signals 34
3.2 Polarization values for glycerol and isopropanol 38
3.3 Schematic of future monochromator based detector 39
3.4 Pinhole sizes from FDM and SLA printers 39
3.5 Schematic of future monochromator based detector (version 2). 40

A.1 Detector schematic (current build). 49

Chapter 1

Introduction

1.1 Motivation

Capillary electrophoresis (CE) is a popular separation technique due to its rapid separation ability for volume limited samples. Challenges arise however due to its low resolution for analytes of similar or nearly identical electrophoretic mobility, such as poly ethylene-oxide (PEO) and poly(dimethylacrylamide-co-allyl glycidyl ether) (EpDMA).[28] However electrophoretic resolution of multiple analytes can be achieved by Fourier transform capillary electrophoresis (FT-CE) or immunoassays (IA) with multispectral fluorescence detection, both of which would require an array of multiple detection points for analyte interrogation. With a detection array, analyte peaks will produce a periodic signal in an electropherogram to create a frequency dependence for Fourier transform (FT) analysis. Multispectral fluorescence allows for resolution of analytes without the need for electrophoretic resolution by probing different fluorescent wavebands. There is also an advantage for simultaneous secretion profiling of biological samples in immunoassays. Designing such a complex device would be time consuming and labor intensive with traditional fabrication techniques such as micromachining or chemical etching.[21] However, this could be remedied by use of 3D printing fabrication technology to reduce the time and effort needed to create a detection system with complex geometric features. The over-arching goal of our research will be the use of 3D printing technology to build a detection array on a capillary for multiple-point detection for future FT-CE and multispectral fluorescence immunoassay applications.

1.2 Capillary electrophoresis

The core basis for this separation technique lies in the determination of size to charge ratio of an ionic species. In a standard capillary electrophoresis (CE) instrument, silica capillaries that have a small inner-diameter are used. The ends of the capillary are both submerged in their own buffer solution, also known as the background electrolyte (BGE), filling the capillary with buffer. The BGE allows the silanol surface of the capillary walls to be deprotonated and form an electric double layer of cations along those walls. This electric double layer is composed of a stern and diffuse layer. Like the name suggests, the stern layer has a strong electrostatic affinity to the negatively charged walls, while the diffuse layer is more dispersed and allowed to freely move across the plane of shear (Figure 1.1). The potential difference on the surface of the walls, between the cations and anions, is known as the zeta potential, ζ. A high-voltage power source is connected to the buffer vials. When a voltage is applied along the capillary, the diffuse layer moves towards the cathode that results in a bulk flow of the solution called the electroosmotic flow (EOF).[17] The velocity of the EOF can be determined by the following equation:

$$v_{EOF} = \left(\frac{\varepsilon\zeta}{\eta}\right)E \tag{1.1}$$

where ε is the dielectric constant of the solution, ζ is the zeta potential, η is the solution viscosity, and E is the applied electric field. The core component of ion separation is their electrophoretic mobility, μ_e. This ion mobility can be defined by:

$$\mu_e = \frac{q}{6\pi\eta r} \tag{1.2}$$

where q is the ion charge and r is the ion radius. The mobility is typically calculated in units of $cm^2/V\bullet$s. The electrophoretic mobility of the ion can be used to determine its velocity under the applied electric field by the following:

$$v = \mu_e E \tag{1.3}$$

The velocity of the EOF is much greater than the velocity of the ion, so as the solution moves towards the cathode, the smallest, most positive ions will travel the fastest while the largest and most negative ions will be the slowest. This separation excludes neutral species, as they are not affected by the field.

1.3 Fourier transform electrophoresis

In Fourier transform theory, any periodic function, h(t), can be described as a series of an infinite sum of sines and cosines, known as the Fourier series for a period between -π and π[3]:

$$h(t) = \frac{a_0}{2} + \sum_{r=1}^{k} a_r cos(rt) + b_r sin(rt) \tag{1.4}$$

$$a_0 = \frac{1}{\pi} + \int_{-\pi}^{\pi} h(t)dt \tag{1.5}$$

$$a_r = \frac{1}{\pi} + \int_{-\pi}^{\pi} h(t)cos(rt)dt \quad r = 1, 2, ... \tag{1.6}$$

$$b_r = \frac{1}{\pi} + \int_{-\pi}^{\pi} h(t)sin(rt)dt \quad r = 1, 2, ... \tag{1.7}$$

where r is the integer number of cycles. Here, a periodic signal in the time domain, can be represented in the frequency domain, H(f), and vice versa by the Fourier transform (FT) function:

$$H(f) = \int_{-\infty}^{\infty} h(t) \cdot e^{-2\pi i f t} dt \tag{1.8}$$

FT is commonly used as a method to enhance a signal from a high noise environment, by separating the frequency components that constitute the signal and noise. Such a process can be applied to analytical separation techniques such as CE.

In 1999, Manz and his team proposed work for Shah convolution Fourier transform (SCOFT) detection for electrophoresis separations.[16] Here they micromachined an electrophoresis chip with a chromium mask that consisted of both buffer and sample channels to pass through a single channel with 55 detection slits. Using laser induced fluorescence (LIF), they aimed to improve resolution between two analytes of similar electrophoretic mobilities, fluorescein and fluorescein isothiocyanate (FITC). As an injection plug of sample passed through each detection point in the time domain, a profile of their frequency dependence could be obtained through Fourier transformation. The advantage to their technique was resolution from baseline drift as well as line noise, however signal-to-noise (S/N) ratio was limited due to inefficient optical design. Electrophoretic resolution between both analytes were also low due to not being able to achieve a small enough spatial resolution of the slits without sacrificing a sufficient amount of sensitivity. Almost a decade later the Chiu group [5], performed similar work and created a microfluidic device for CE separations consisting of 5 detection channels in parallel with one another to carry out a series of simultaneous injections and enabling periodic detection of FITC-labeled amino acids. Conversion of electropherograms into the frequency domain facilitated noise filtering and increased S/N as well as separation resolution, showcasing the success of Fourier transform detection in Manz's work. This study however was also not optimized for reduced detection limits. The work we propose here will be developing an affordable 3D printed fluorescence detector for capillary separations to enable resolution of small complex geometric features for miniature optics that will improve the efficiency of the optical design to increase S/N in fluorescence measurements. This will also allow us to minimize the cost and size of our detectors and enable a greater range of detection points for the FT-CE method.

1.3.1 CE immunoassay

Capillary electrophoresis-immunoassays (CE-IA) combine the selectivity of immunoassays with the rapid analysis of CE separations, without the need for lengthy and inefficient phase separations. The first separation of an antibody-antigen complex by CE was introduced by Nielsen followed by Shultz and Kennedy's development of competitive and non-competitive CE-IA modes.[30] In non-competitive IA, a known quantity of excess fluorescently labeled

antibody is added to the sample to form a complex with the analyte of interest. CE separation will reveal two peaks in the electropherogram where one is related to the free labeled antibody and the other the formed complex. Quantification of analyte is directly related to quantity of labeled antibody available in the mixture. In a competitive CE-IA, if labeled antigen and a limiting amount of antibody are added to a sample with another antigen, then both antigens will compete for binding with the unlabeled antibody based on its availability. The CE separation will display two peaks, one for the labeled complex and one for the labeled antigen. The sample antigen will decrease the amount of labeled complex formed to increase the amount of free labeled antigen and allow for quantification with comparison of the peaks with standards. In addition to eliminating the need for phase separation, CE-IAs offer efficiency advantages via improved ability for automation, and rapid separation of antigen, antibody, and complexes which can be achieved in seconds to minutes.[20, 32] Additionally, CE has a very low sample volume requirement (ca. $1 - 10$ nL) while maintaining detection of trace sample amounts and eliminating the need for sample preconcentration techniques.[32]

1.3.2 Multispectral fluorescence detection mode

One of the most common modes of detection in CE is laser-induced fluorescence, which can provide limits of detection approaching single-molecule levels.[14] Due to the highly selective detection of CE-IAs, via both immunoaffinity and selective fluorescence detection, multispectral fluorescence detection is required to enable simultaneous detection of multiple analytes by CE-IA. Roper and colleagues showcased this technique with a two-color fluorescence CE-IA for simultaneously assaying the secretion profiles of insulin and glucagon from islets of Langerhans.[22, 23, 27] Although this multispectral detection approach enables the profiling of multiple analytes with the sensitivity and efficiency advantages of CE-IA, the cost and complexity associated with multiple laser excitation sources and complex optical filtering arrangements has limited the adoption of this powerful technique.

1.3.3 Fluorescence polarization

Polarized light enables photoselection when the fluorophore's transition dipole is in alignment with the polarization axis. In the case that a fluorophore is static, if vertically polarized light is absorbed, then the resulting emitting light will retain its polarization axis. However, because molecules rotate and tumble in space, the polarization axis will change, by the time light is emitted. This depolarization rate is dependent on the molecule's angular velocity and fluorescence life time. This phenomenon is known as fluorescence polarization.[25] If a fluorophore is excited by vertically polarized light, the polarization can be quantified by the following equation:

$$P = \frac{I_V - I_H}{I_V + I_H} \tag{1.9}$$

where I_V is the intensity of emission passing through a vertical polarizer with respect to the incident polarization, and I_H is the intensity of emission that is horizontally polarized. The polarization range of values are -1 to +1. In the case that the polarization of a molecule is -1, the molecule is completely polarized perpendicular, or depolarized, to the incident polarization. When polarization is +1, the molecule is completely polarized parallel to the incident polarization. When polarization is 0, then emission is not polarized. In the absence of rotation, such as when a fluorophore is placed in a very viscous or frozen solution, P_0, the intrinsic or limiting polarization can be measured by the following equation:

$$\left(\frac{1}{P_0} - \frac{1}{3}\right) = \frac{5}{3}\left(\frac{2}{3cos^2\phi - 1}\right) \tag{1.10}$$

where ϕ is the angle between the absorption and emission dipoles. Polarization of a molecule can also be related to the its intrinsic polarization and excited state life time:

$$\frac{1}{P} - \frac{1}{3} = \left(\frac{1}{P_0} - \frac{1}{3}\right)\left(1 + \frac{3\tau}{\rho}\right) \tag{1.11}$$

where τ is the excited state life time and ρ is the Debye rotational relaxation time. The rotational relaxation time is the time in which a molecule rotates about 68.42° which for a sphere is:

$$\rho = \frac{3\eta V}{RT} \tag{1.12}$$

where η is the solution viscosity, V is the molar volume of the rotating molecule, R is the universal gas constant, and T is the temperature. This means that larger molecules rotate more slowly and thus retain more of its polarization, while smaller molecules rotate faster and are more depolarized. Fluorescence polarization is commonly seen in the field of biology, typically as a method to observe protein binding and size determination.[9, 13, 15, 19]

1.4 Frequency modulation

Frequency modulation (FM) is a common technique used in both telecommunication systems and spectroscopic techniques. As the name suggests, FM modulates the frequency of a carrier signal with a modulator to improve signal detection in high background noise environments. Noise is uniformly distributed across the spectrum of the signal, which indicates that the signal will not be affected by frequency variations from noise. The signal will be affected by amplitude variations however.[11, 26, 29] During modulation, the FM signal for an optical wave at time, t, can be be defined by:

$$E = E_0 \cdot e^{[j(2\pi f_0 t + \beta sin(2\pi f_m t))]} \tag{1.13}$$

$$\beta = \frac{\Delta F}{f_m} \tag{1.14}$$

where E_0 is the instantaneous of the wave, f_0 is the center frequency, j is the Bessel function, β is the modulation index where ΔF is the max frequency deviation, and f_m is the modulating frequency. In fluorescence spectroscopy, the pulse of the excitation source is modulated with a sinusoidal pattern of known frequency. This enables the fluorescence signal in the time-domain to follow the same sinusoidal pattern. An FT can then be used to transpose the signal in the frequency spectrum. The FM signal intensity in the frequency-domain can be measured at the specified modulation frequency and will also be resolved from any out-of-frequency noise patterns.

1.5 3D printing

3D printing is becoming a popular fabrication tool in a variety of research disciplines including microfluidics.[21] 3D printing facilitates fast and affordable construction of complete analytical devices rather than a tool used for prototyping purposes. One of the major advantages of 3D printing is that it offers single-step production of complex geometries that would be difficult to achieve with other fabrication methods such as injection molding [6] and micro-milling [8]. Some of the modes of 3D printing include: fused deposition modeling (FDM),[2] stereolithography (SLA),[1] and polyjet printing.[7] Work-flow of these additive manufacturing methods begins with a 3D drawing using a computer-aided design (CAD) software. The model is exported to a 3D slicing software that translates the model into stacked individual layers for 3D printers.[7] Resolution of FDM, SLA, and polyjet printing are on the order of 250, 25, and 45 μm in the XY-plane and 178, 6, and 28 μm in the Z-direction, respectively.[21, 24, 38] Roux and colleagues demonstrated their ability to produce 25 μm (XY) by 27 μm (Z) microchannels with a digital light processing-SLA printer to facilitate the encapsulation of neuronal stem cells.[4]

3D printing offers much versatility in the world of fluidics, such as Renaud's SLA printed microfluidic device that facilitated mixing via rigid elements to split, combine, and rearrange component flow-lines. [10] DNA assembly work was also demonstrated realizing the potential for synthetic biology.[31] However, less attention has been focused on the advantages of 3D printing in producing components peripheral to the central fluidic devices, such as optical detection systems, which combine to form the complete instrumental analysis system. Prikryl and Foret demonstrated the 3D printing of an LED-induced fluorescence detection system for CE detection of oligosacharides.[33] As their work illustrates, 3D printing can enable low cost, high precision analytical instrumentation, even without providing the spatial resolution needed for high precision microfabrication of microfluidic devices. Significantly more work is left to be done in realizing the full potential of 3D printing as a tool for developing optical detection systems in CE and other capillary-based flow techniques. In chapter 2, we will explore the idea of using 3D printing as a method for designing a miniaturized and inexpensive fluorescence detector.

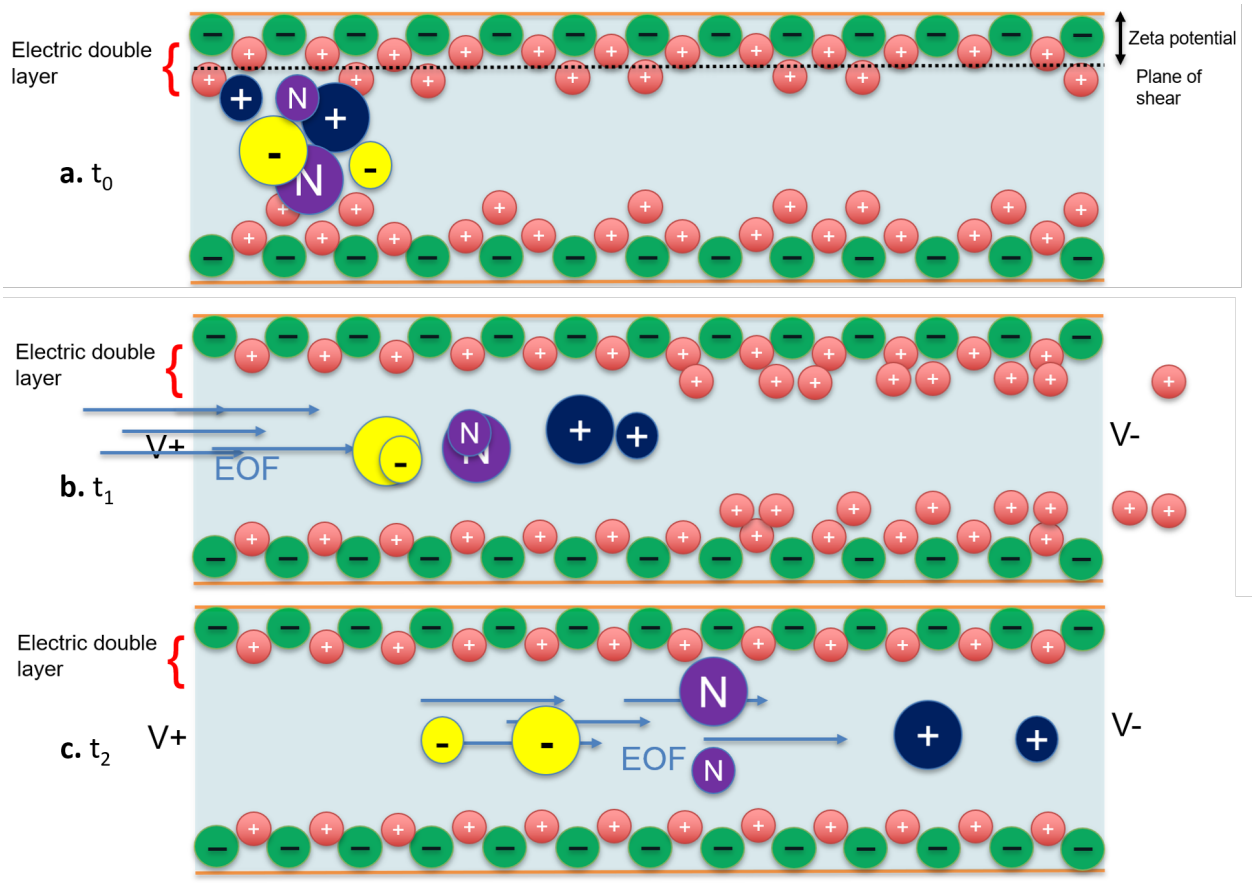


Figure 1.1: a-c) A diagram of CE separation at different points of time under an applied voltage.

Chapter 2

Development of a miniaturized fluorescence detector for CE

2.1 Introduction

Multispectral-fluorescence gives us the ability to detect multiple analytes in a separation, even when those analytes are not resovled by the separation process. A detector that provides multiple modes of fluorescence detection would typically require multiple laser excitation sources, but the cost burden of such an arrangement has limited the adoption of multispectral-fluorescence detection for CE. Light emitting diodes (LEDs) offer an alternative to lasers because they are less expensive, consume less energy, and have a wider range of wavelengths to select from for efficient dye excitation.[34] A comparative analysis of laser and LED induced fluorescence in a CE instrument was done by the Couderc group, showcasing a higher signal-to-noise ratio detection from LED excitation at 450 and 530 nm vs. laser excitation at 410 and 488 nm, for human immunoglobulin labeled with naphthalene-2,3-dialdehyde (NDA; λ_{Ex} maxima: 419 nm) and 5-carboxytetramethylrhodamine succinimidyl ester (5-TAMRA.SE; λ_{Ex} maxima: 546 nm) dyes, respectively. This was due a higher spectral overlap of LED excitation wavelength with the dye's excitation maxima.[34]

In our earlier work, a miniaturized 3D printed detector that incorporated an LED as the excitation source was designed around capillary-based separation techniques.[12] This included a design for the purpose of integration into a commercial CE instrument. One key

challenge throughout the development of this detector was to minimize the noise produced from aberrant light scatter from the excitation source. This scatter is due to the refraction of light passing through the interface of two materials with differing refractive indices, as well as reflection at the interface. This phenomenon mostly occurs at the interface of the capillary and is the main contributing factor of noise.

To address this, the detector was optimized to incorporate multiple optical components within the detection body. The excitation and emission paths are positioned 90° from each other with the capillary detection window located at the intersection of the two, as shown in Figure 2.1 A. This would help maximize the amount of fluorescence being collected while minimizing the collection of excitation light. A pinhole collimator was integrated into the printed detector to spatially reject uncollimated LED light. This allowed collimated light to be incident upon the detection window of the capillary. Fluorescence was collected at the focal point of a ball lens and collimated towards a fiber bundle adjacent to a PMT module. A scaling factor was applied to the detector CAD model to combat thermal expansion effects. Scatter remained a large component of our system, so we have decided to use a lock-in-amplifier (LIA) to modulate our excitation source and demodulate the PMT signal before data acquisition. While beneficial to lowering the background of our fluorescence measurements, a lock-in-amplifier is expensive and an encumbrance to miniaturization.[12]

With our work, we aimed to improve upon the original design of the detector with the goal of reducing scatter. We attempted a dual lens system oriented in a confocal arrangement to increase the S/N by resolving focused emission through a pinhole while also rejecting unfocused excitation scatter. Polarized scattered light via use of linear polarizers were also explored to reduce scatter intensity and preserve fluorescence along with an additional reflector element to increase fluorescence intensity. In addition, we explored digital filtering algorithms to increase S/N and reduce complexity and cost as an alternative to the LIA. Concentration calibration curves of fluorescein in sodium tetraborate buffer were obtained to characterize the limit of detection (LOD) with each optical component.

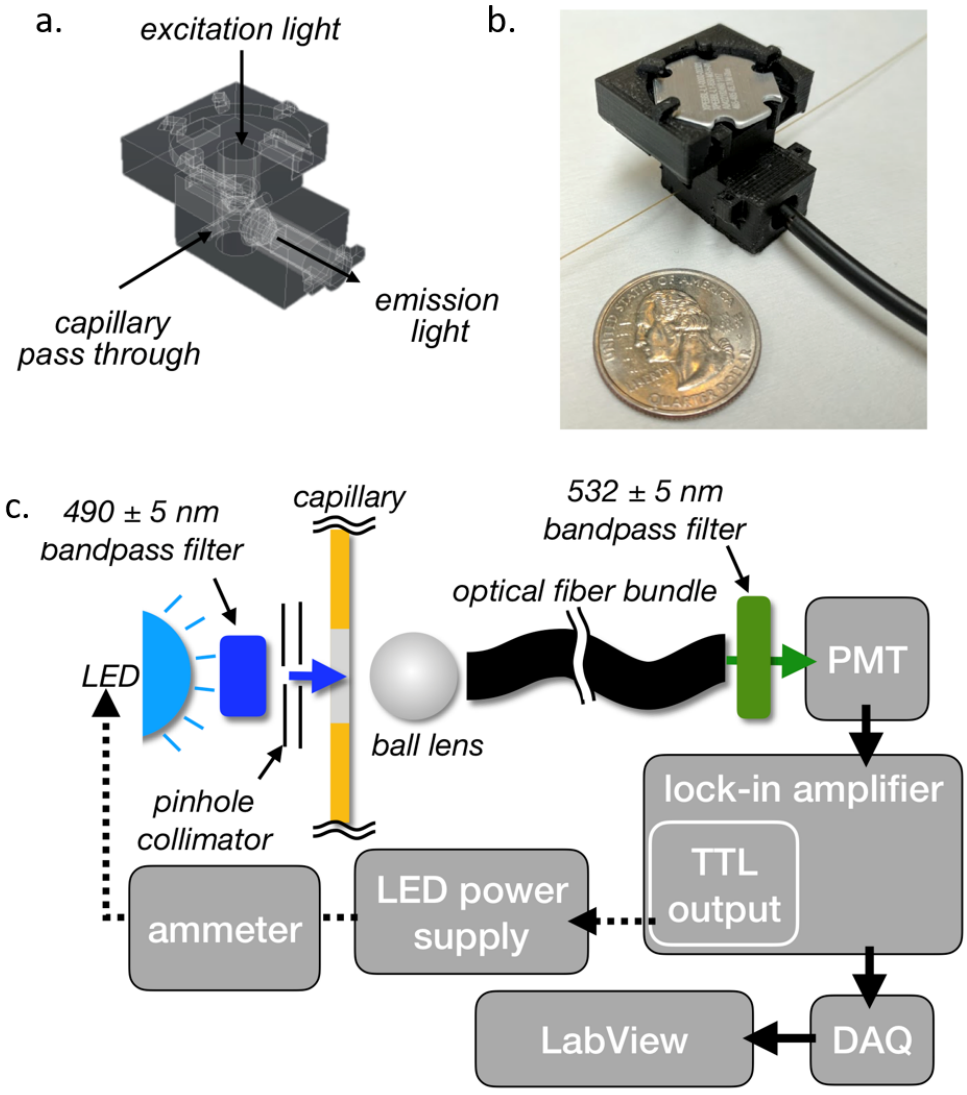


Figure 2.1: a) The excitation and emission beam path are orthogonal to each other where the capillary is placed. b) A photograph of the miniature scaled of the detctor (6.3 cm^3) is placed next to a quarter for scale. c) A schematic of the previously designed detector.[12]

As shown in Figure 2.2 a., fluorescent rays originating at the focal point of the ball lens are collimated into a fiber optic bundle. A second ball lens, as shown in Figure 2.2 b., can refocus collimated light into a small pinhole, before approaching the fiber. In this process, out-of-focus scattered light will not collimate through the first lens, but instead will be refracted at a different angle and be absorbed within the walls of the detection body. This confocal design serves as a spatial rejection element for out-of-focus scatter while preserving the focused fluorescence. Optimal performance of the system requires precise positioning of the capillary, lenses, and pinhole, where a deviation in any element will increase focusing of scatter and reduce collection of emission. Performance is also reliant on pinhole diameter and thickness where smaller pinholes increase spatial rejection of out-of-focus scatter and thinner pinholes increase in-focus light to pass through.

A linear polarizer is used to control the polarization axis of the excitation source before approaching the silica and buffer interface. The scattered incident light maintains its axis of polarization, and a second polarizer in the orthogonal orientation is used to block scattered incident light. Polarization axis of the emission will change due to the rotating motion of the fluorophore and allow some emission light to be preserved. The rate of this effect varies depending on the size of the fluorophore. Smaller molecules often rotate more rapidly and retain its incident polarization for a shorter period of time, thereby allowing more emission light to pass the second polarizing filter. Larger molecules however, produce the opposite effect and a lower intensity of emission will be preserved. The primary benefit of polarization is the rejection of scatter, but the differences in polarized light intensities could be beneficial for fluorescence polarization measurements in the future.

Improved fluorescence collection via cylindrical reflector

As is typical for most detection systems, the original optical design captured fluorescence emission from only the lens-directed front face of the capillary. Part of our design includes a cylindrical exit hole for excess excitation light. The geometry of the hole can be advantageous when combined with a reflection element. A reflecting material such as metalized Mylar is positioned behind the capillary against the exit hole, such that the material will conform to the shape of the cylinder. The capillary will be placed at the focal point of the lens

and the center of curvature of the mirror, where emission light behind the capillary will be reflected by the mirror towards its center and thus the lens' focal point for collimation. Fluorescence collection intensity will be increased while out-of-focus scatter is reflected back into the detector cavity, as shown by Figure 2.3 b.

2.2 Material and methods

2.2.1 Reagents

Flourescein disodium salt and sodium tetraborate were purchased from ThermoFisher Scientific (Waltham, MA). Borate buffer solution (10 mM) was prepared using water from Milli-Q purification system (Millipore, Bedford, MA) and pH adjusted to 8. Fluorescein standards were diluted with the buffer solution from a range of 10 μM-70 nM. Fresh solutions of buffer and standards were prepared each month.

2.2.2 Device fabrication and assembly

A QIDI technology I Dual Extruder Desktop 3D printer was used to print the detection body. The printer was loaded with a 1.75 mm diameter acrylonitrile butadiene stryene (ABS) filament spool and extruded through a 0.4 mm nozzle head. The detector model was designed in the AutoCAD software and scaling factor of 1.125 was applied to the model excluding the LED holding head. The CAD model was exported in a stereolithography (.stl) file format, and transferred to a slicing software, Replicator G, to be rendered as a G-code. Extrusion temperature was adjusted to 260 °C and platform bed to 110 °C. Additional software parameters include a 50% object infill, a 0.1 mm layer height, and a 30 mm/s feedrate. A 4 mm glass plate was used as the build platform and layered with hairspray (Aqua Net, Lornamead, Inc, Tonawanda, NY) to facilitate print adhesion of the first layer.

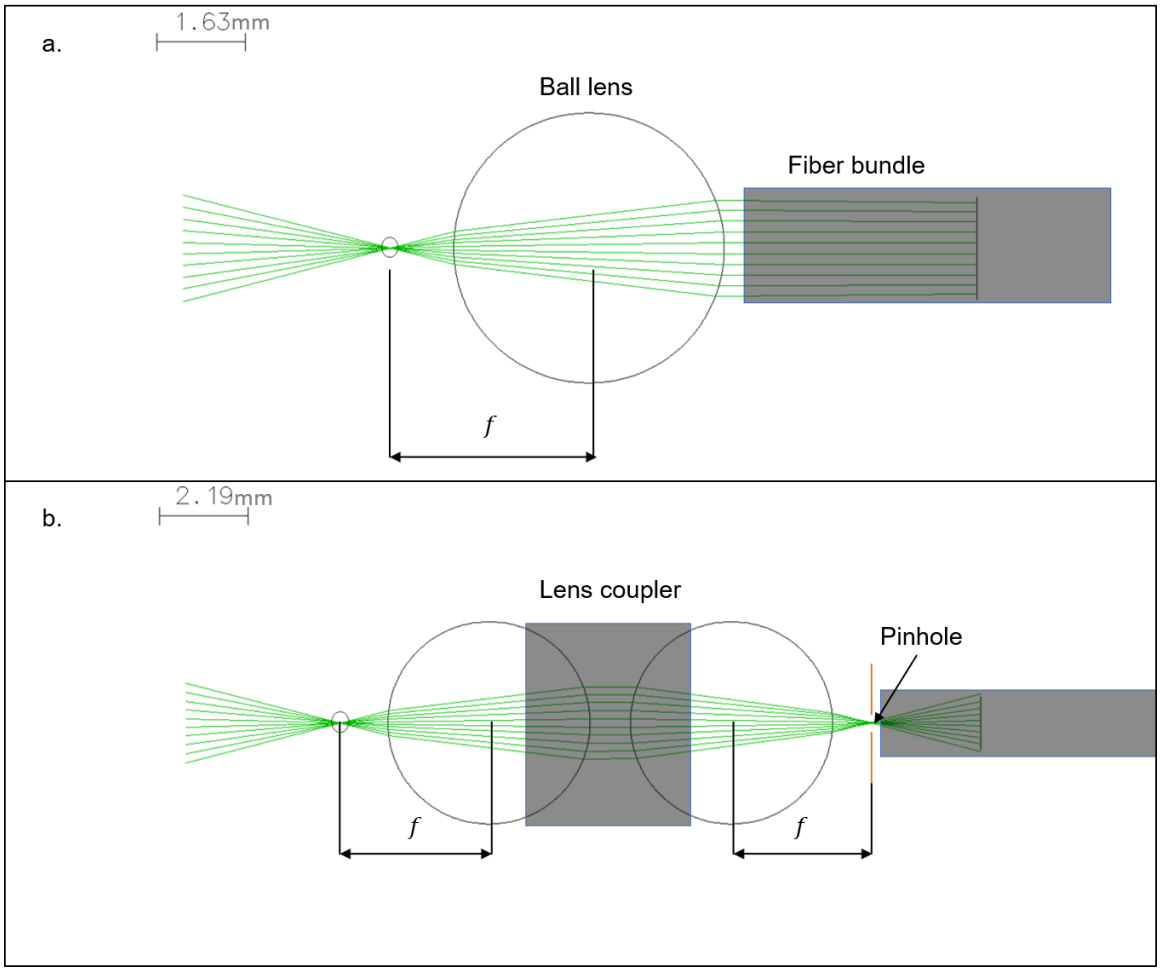


Figure 2.2: a-b) A mechanistic diagram of a single and dual ball lens system, respectively, where f is the focal point of the ball lens. A capillary is centered around the focal point to allow beam collimation into a fiber optic bundle. In the case of a second ball lens, a pinhole is aligned with the focal point of the second lens to allow collimated light to be focused into the fiber.

Assembly of the device includes a high power, single color 465-485 nm LED (XPEBBL-L1-0000- 00301-SB01, Opulent Americas, Raleigh, NC), with connection leads via spring-loaded contact probes (0900-3-15-20-75-14-11-0, Mill Max, Oyster Bay, NY) to a DC adjustable power supply (TP3003E, TekPower, Montclair, CA). A 3 cm detection window in a 100 μm i.d./360 μm o.d capillary is created by burning the polyacrylamide coating off the capillary and cleaned with isopropanol. The capillary is inserted into the pass-through with the window aligned to the center of the pinhole collimator. The capillary then is secured by 3D printed clips clamped down with binder clips. Excitation light passes through a 490±5 bandpass filter (W4489, Omega Optical, Inc., Brattleboro, VT) is incident on the center of the capillary detection window. Fluorescence emission is collected via a single 5 mm BK-7 glass ball lens (43712, Edmund Optics Inc., Barrington, NJ) that is coupled to a fiber optic bundle (02-540, Edmund Optics Inc., Barrington, NJ), and transmitted through a 532±5 nm bandpass filter (FL532-10, Thorlabs Inc. Newton, NJ) before entering a photo multiplier tube (PMTSS2, Thorlabs Inc., Newton, NJ). An additional ball lens is coupled for confocal system studies along with an integrated small pinhole(0.5 mm). Signal is collected via a data acquisition device USB-6001 for the lens alignment study and USB-6210 (National Instruments, Austin, Texas) for all other LOD experiments. See appendix Figure A.1 for an assembly diagram.

For polarization studies, as shown in Figure 2.4 the detection body allows access for linear polarizers (LPVISE2X2, Thorlabs Inc., Newton, NJ) in both the excitation axis beneath the band pass filter and the emission axis preceding the ball lens. A laser cutter (VLS 2.30,

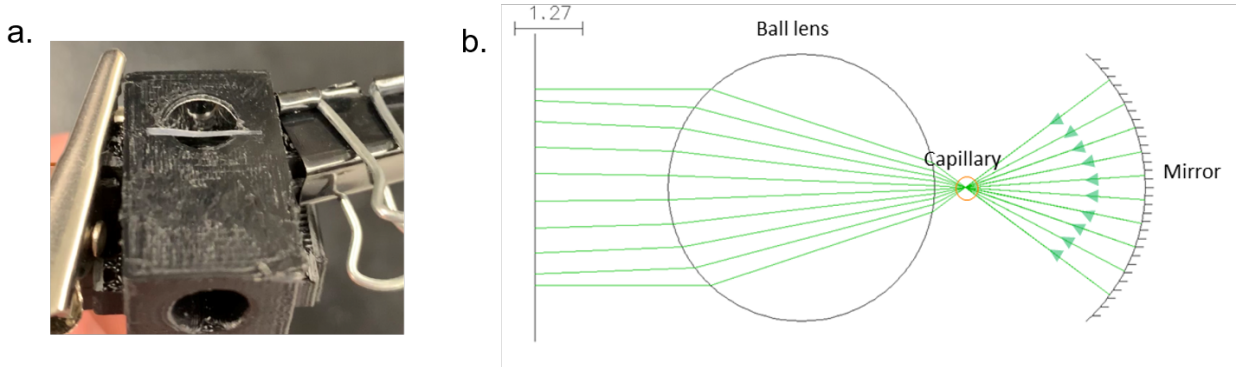


Figure 2.3: A) A photograph of the Mylar material placed behind the capillary. B) A mechanism for improved fluorescence collection using the reflector.

Universal Laser Systems Inc., Scottsdale, AZ) was used to cut appropriately sized filter (6 mm diameter for excitation and 7.5 mm × 5.5 mm for emission) to be fitted to the detector. A Metalized Mylar sheet metal (Vivosun, Los Angeles, CA) cut with the laser cutter (10 mm × 6.6 mm) was placed into the exit cavity of the detector where the center of curvature of the mirror is aligned with the focal point of the ball lens, as shown in 2.3 a.

2.2.3 Calibration curve development

Calibration curve experiments were carried out by pressure flow of borate buffer for 20 seconds and quickly exchanging to fluorescein for an additional 20 seconds. Solution flow is facilitated by syringe pulling. LED current was optimized for maximum S/N output from buffer to 10 μM fluorescein. Data acquisition was performed using LabVIEW code written in lab, where the collection frequency of the signal was 5 Hz. Signal-to-noise was determined by the average fluorescent signal over the standard deviation of the background electrolyte. Limit of detection calculations were determined when the concentration of the sample has a S/N of 3.

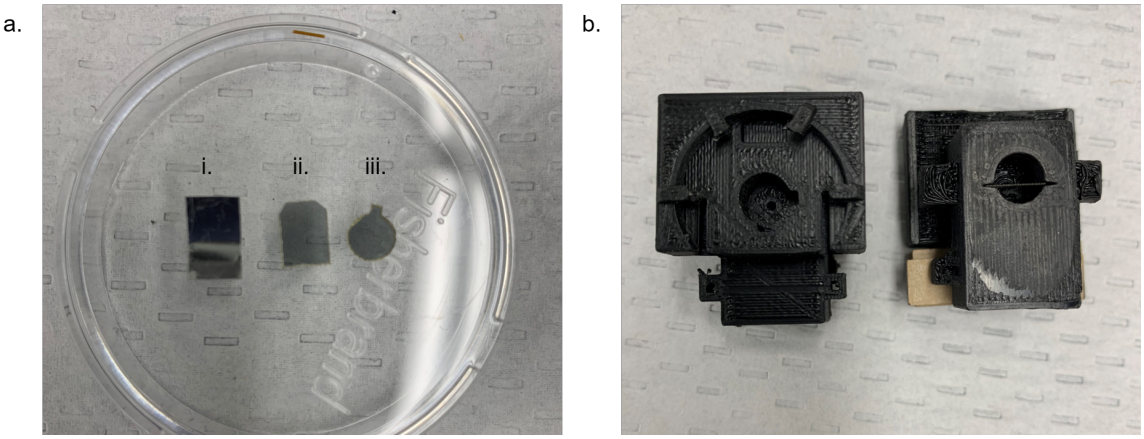


Figure 2.4: a) From left to right is a cut out of the i.) reflector, ii.) the polarization filter used for the emission axis, and iii.) the polarization filter for the excitation axis. Corners are cut to indicate the direction of polarization for the emission axis and the small flat square in iii. indicates the direction of polarization in the excitation axis. b) A photograph of the placement of the polarizers.

2.2.4 LED frequency modulation

Modulation of the excitation source was performed using another written LabVIEW code. A carrier frequency of 100 Hz was applied to the excitation source via a USB-6001 while a USB-6210 was used to demodulate and collect signal. The signal was observed at a 20 Hz bandwidth.

2.3 Results and discussion

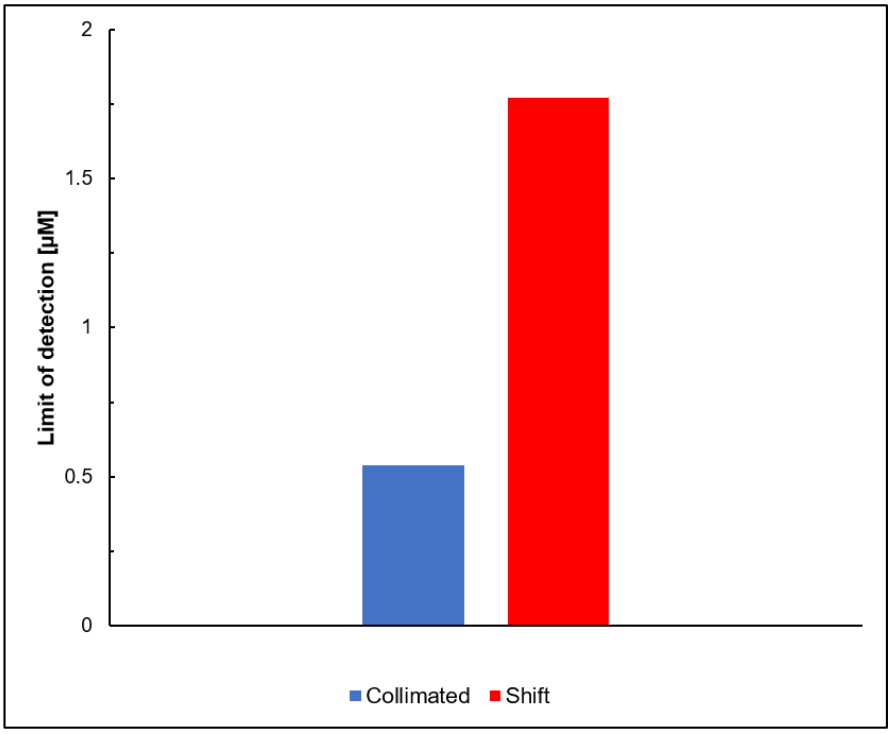
2.3.1 Ball lens alignment

Figure 2.5 shows a comparison of LODs for the detection system where fluorescence is emitted at the focal point of the ball lens and one where the lens is shifted forward 3.0mm. The LOD values were increased by a factor of 3 for a shifted lens. When the lens is misaligned, less emission light originating at the focal point will be collimated towards the fiber. To further explore the collection of emission and rejection of scatter, a second ball lens was introduced into the system.

2.3.2 Confocal lens system

As shown in Figure 2.6, the highest S/N is produced from a lower range of currents used to power the LED and determined to be 50 mA for a single lens system and 70 mA for a dual lens system. Light intensity increases proportionally with the current applied to the LED. As intensity increases, more scatter was introduced to the system creating a larger background. Additionally, at higher currents output by the LED for the dual lens system, Joule heating increased and began to melt and warp the plastic. The warping effect caused optical misalignment of the bandpass filter and the pinhole collimator, effectively reducing the S/N detected.

a.



b.

	LOD [µM]
3.0 mm Shift	1.7± 0.1
Collimated	0.5± 0.06

Figure 2.5: Limit of detection comparison for a collimated vs. shifted ball lens.

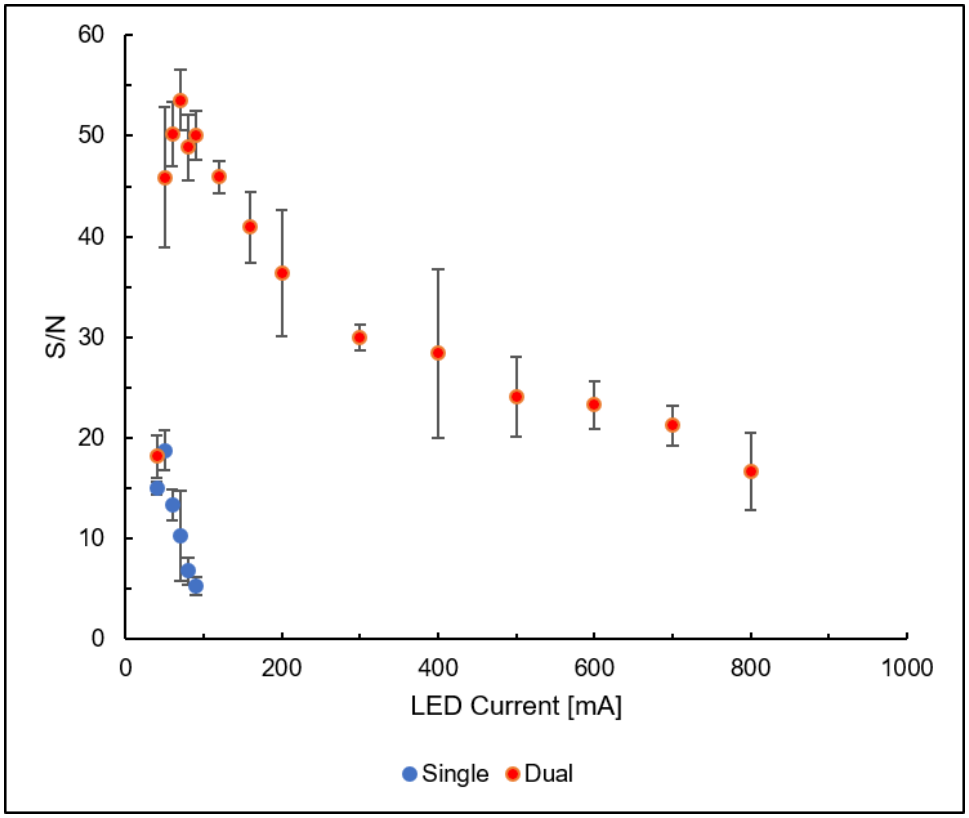


Figure 2.6: Optimization of LED current to determine a maximum S/N response for both single and dual lens systems.

Figure 2.7 shows the system performance between the two different systems of lenses. S/N diminished by a factor of approximately 7 with the addition of a second lens. The added pinhole that proceeded the fiber decreased the total light intensity collected by the PMT but was observed to decrease more fluorescence than scatter. The Accurate alignment of the two lenses and pinhole as well as the depth and size of the pinhole is critically important for this system to work. While 3D printing provides the advantage of low cost modeling, there is still an uncertainty in the dimensions of each print. These uncertainties are due to the extrusion nozzle size (0.4 mm) of the printer and thermal expansion effects of the plastic. Smaller nozzle sizes will reduce printed layer height and increase detail in the horizontal plain. Thermal expansion will hinder the ability to achieve smaller features such as small slits and pinholes because they will expand and close after they are printed. Because of this, a wall thinner than 0.5 mm could not be achieved with the printer. A study comparing printed pinhole thickness to their CAD model was performed to observe the differences in thickness of each print, as shown in Figure 2.8 a. There also appeared to be roughness in each print even when printing replicates of the same sized depths which increased the difficulty to achieve uniformity. Depths printed below 0.5 mm displayed areas of structural weakness by leaving unintended holes in the surface as shown in Figure 2.8 b. The QIDI printer lacked the required resolution to achieve this precise alignment hindering the effective focusing of emission and rejection of scatter.

2.3.3 Linear polarization filter characterization

Linear polarization filters require positioning of the angle to accurately control the polarization axis of light. However when compared to lenses, polarizers do not have a focal point and thus do not require precise spatial positioning like the lenses. We performed a study to determine the amount of scatter collected from the interface of the capillary under an LED current of 50 mA. Nine configurations of filters were used including a control for no polarizers, as shown in Figure 2.9. Each polarizer was placed with its polarization axis parallel or perpendicular with respect to the capillary axis. The addition of a single filter in either the excitation or emission axis effectively reduced the scatter intensity by up to 52.5%. Polarization filters included in both excitation and emission paths with aligned polarization

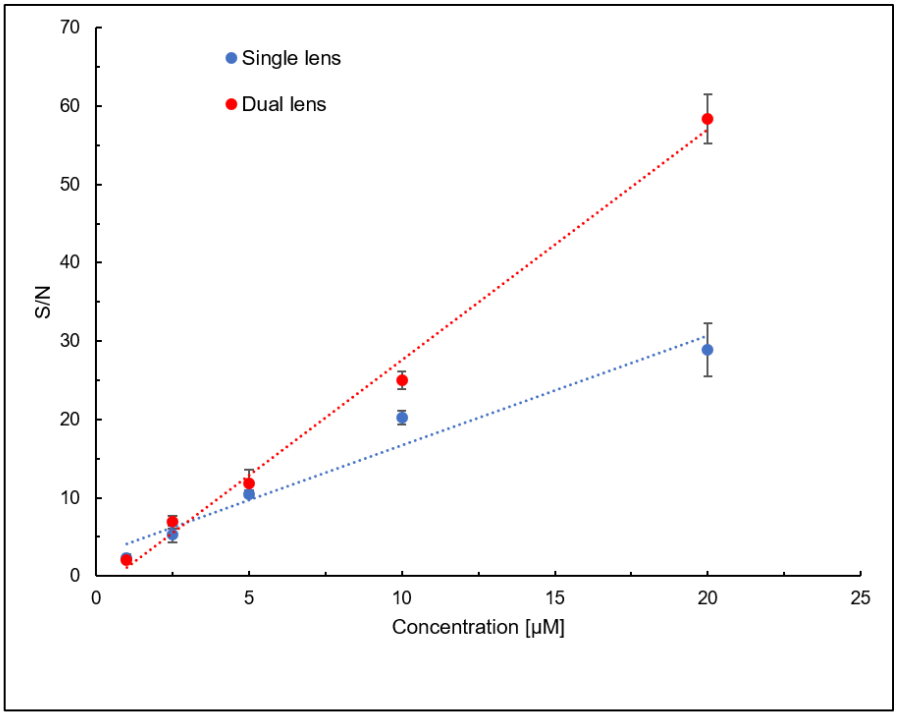
axes, either ∥+∥ or ⊥+⊥ with respect to the capillary axis, did not reduce the intensity of collected scatter with statistical significance as compared with single polarizer experiments. When two filters are oriented with polarization axes orthogonal to one another, scatter was reduced by a factor of 39 in the ∥+⊥ configuration. Limit of detection calculations for dual polarizer systems under the same LED current parameters were studied and are shown in Table 2.1. Interestingly, maximum scatter rejection was achieved when excitation polarizer was aligned parallel with respect to the capillary axis. We hypothesize that this is an artifact of the cylindrical geometry of the capillary. In this orientation, a greater surface area of the capillary wall was co-linear with respect to the polarization axis of the excitation source, resulting in a greater effective surface area in which scattered light can preserve the polarization axis. More work is needed to confirm this mechanism, but results of this study demonstrate a distinct advantage in terms of achievable LOD for (∥+⊥) as compared with (⊥+∥).

The previous LOD comparison of the different polarizer systems were operated under an applied LED current of 50 mA. S/N was further improved by determining optimal current conditions (100 mA) for ∥+⊥ by using the same LED optimization protocols stated previously. Figure 2.10 displays a S/N of 70±0.001 nM totaling to a 13-fold increase in S/N from the original design.

Table 2.1: LOD of dual polarization filters with no filters used as a control with an LED current of 50 mA.

Type	LOD [μM]
No filter	1.3±0.05
∥+∥	2.0±0.3
⊥+⊥	1.6±0.004
⊥+∥	0.4±0.01
∥+⊥	0.1±0.01

a.



b.

	LOD [μM]
Single lens	0.23±0.03
Dual lens	1.6± 0.07

Figure 2.7: LOD comparison for the LED optimized lens systems.

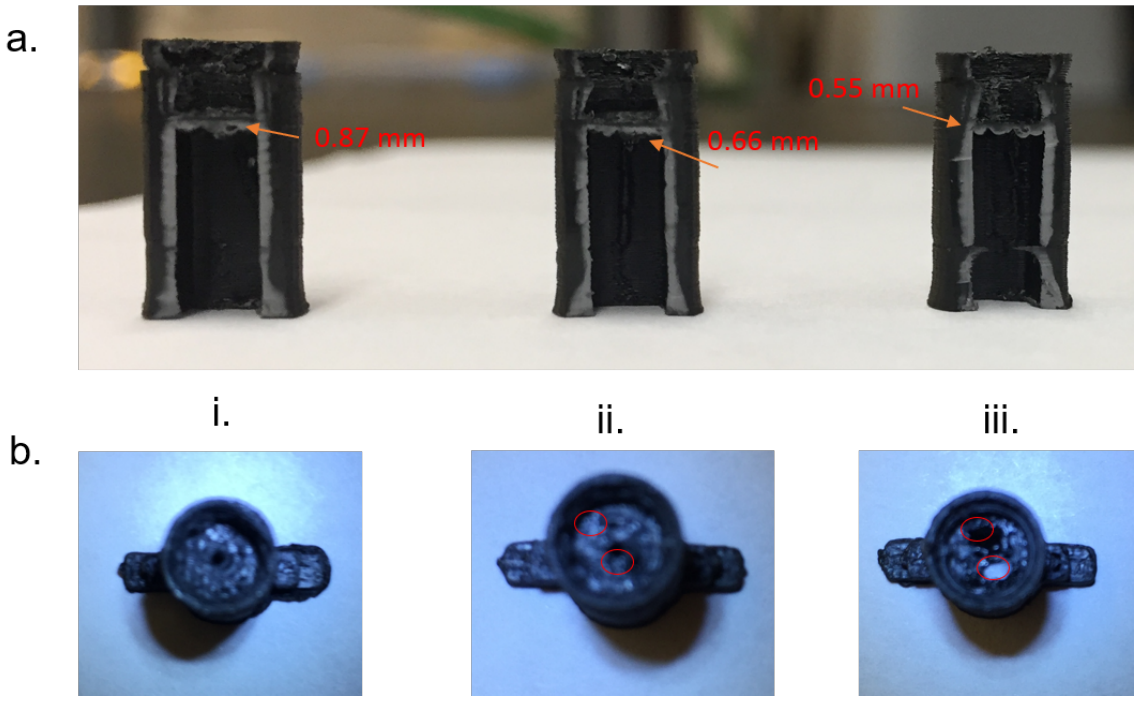


Figure 2.8: A) A cross section cut of pinholes printed at different depths (i.) 0.5 mm, ii.) 0.4 mm, and iii.) 0.3mm) shows the roughness of each print. B) Top down view of pinholes below A)

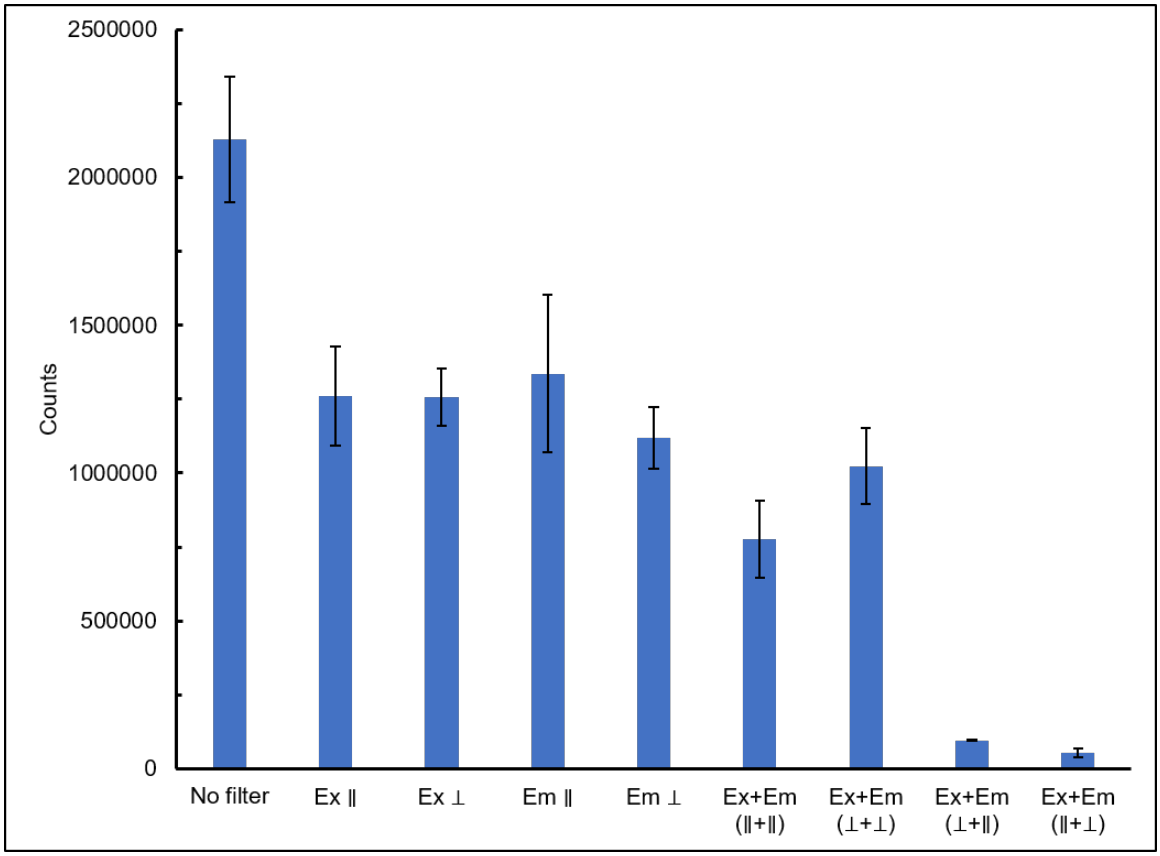


Figure 2.9: Noise determination of light scatter for the detection system with polarizers placed in all orientations in the excitation and emission beam path with no filters used as a control.

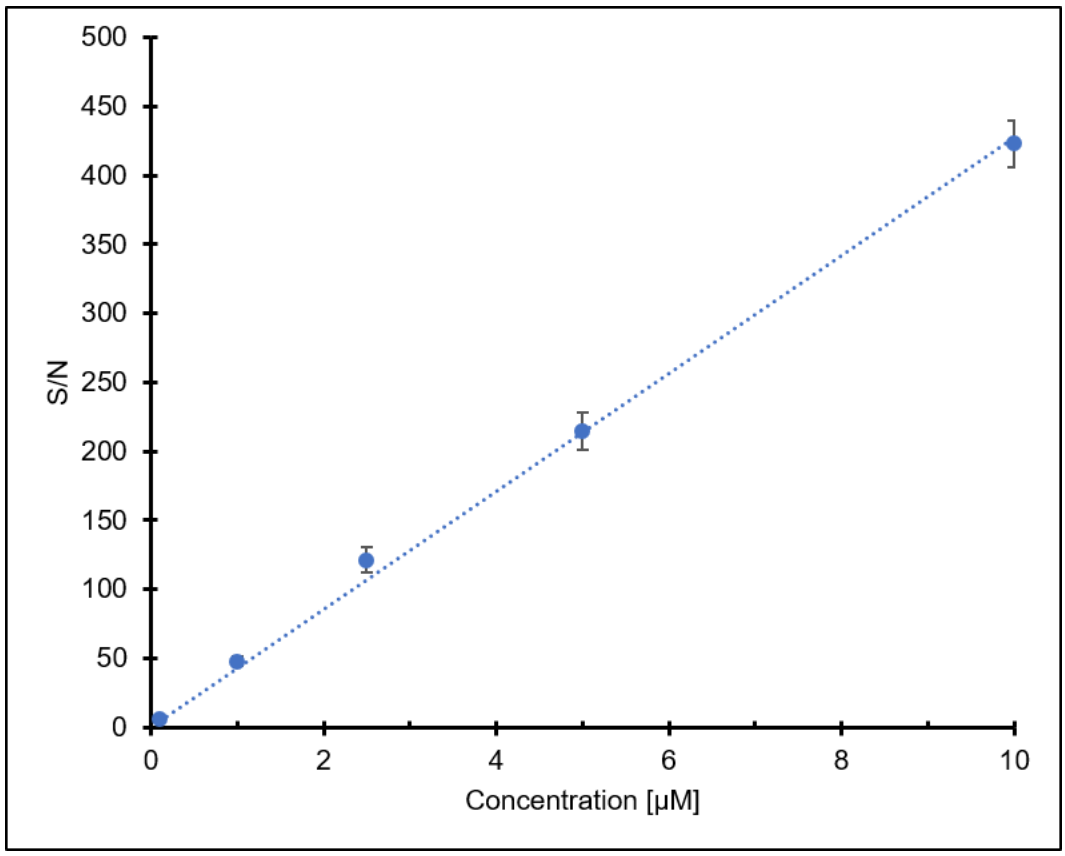


Figure 2.10: LOD of detection system with two polarizers ($\|+\perp$) under optimum LED current conditions.

2.3.4 Improved fluorescence collection by reflection

Commercial mirrors can be large and expensive, but a metalized Mylar reflecting sheet can be used as an alternative in reducing the size and cost of the detector. This is advantageous because smaller and more affordable optical components enable us to minimize the overall cost and size of the detector to be used in an array. However, due to the cylindrical shape of the incorporated reflector, improvement of fluorescence collection is limited to one axis of curvature, whereas a spherical mirror would capture fluorescence emission from a wider area. Figure 2.11 shows a calibration curve with both the addition of polarizers and reflector elements. The current was optimized (110 mA) and LOD of the system was determined to be 20±0.0008 nM. This improvement in S/N was expected due to the increased collection of fluorescence behind the capillary by reflecting in-focus light through the focal point of the ball lens and reducing out-of-focus scatter. Alternatively, it may be that the Mylar reflector acted to refocus scattered excitation light back to the center of the capillary, thereby effectively increasing the intensity of the excitation light. Further work would be needed to determine if this mechanism is present in the current system.

2.3.5 Digital frequency modulation

Following the same optimum LED current of 110 mA, frequency modulated experiments were performed. The modulation frequency was 100 Hz, so Fourier transformation from the time to frequency domain displayed a Gaussian shaped peak centered at 100 Hz. The changes in both the peak area and peak height were measured in response to buffer and fluorescein solution input to determine S/N similar to previous S/N determination protocols. The best S/N performance of the two methods is shown in Figure 2.12. Peak height showed a higher sensitivity calibration curve than peak area which is possibly due to a limited area of integration (20 Hz bandwidth) under the curve. Overall S/N performance was then not improved. As stated previously, most of the noise that is generated is a result of excitation light scatter. The LIA was previously used to demodulate the FT signal to attenuate amplitude variations in noise. However, in this digital filtering system, the transformed data was used to filter out-of-frequency components of the signal to determine S/N. We

hypothesize that when the excitation source is modulated, both the fluorescent signal and scatter are modulated as well and the amplitude variations are retained. This will effectively result in no change in S/N. More studies are needed to observe this effect.

2.4 Conclusion

In this work, lens alignment, polarization, reflective mirrors, and digital filtering were explored with the goal to decrease excitation scatter. Spatial rejection of scatter and focusing of emission could not be realized without achieving the proper lens alignment or pinhole size. Ultimately, this was due to inadequate printing resolution of the FDM printer. Addition of polarization filters could control the polarization axis of scatter and largely reduce it, while both the filters and reflector effectively preserved fluorescence, and increased LOD to a low nM (20$\pm$0.0008 nM) scale. Frequency modulation of the excitation signal proved to be unsuccessful in reducing background because the noise was being modulated along with the emission signal. Further LOD determinations of the different polarization filter configurations could prove to be useful in determining the effects reflected polarized light, in the future. The dual lens system is another configuration that can still be explored with SLA printing technology to further increase optical alignment. The relatively inexpensive design of the detection head allows for a larger array of n detectors on a single capillary without size and cost limitations for future FT-CE and multispectral-fluorescence detection applications.

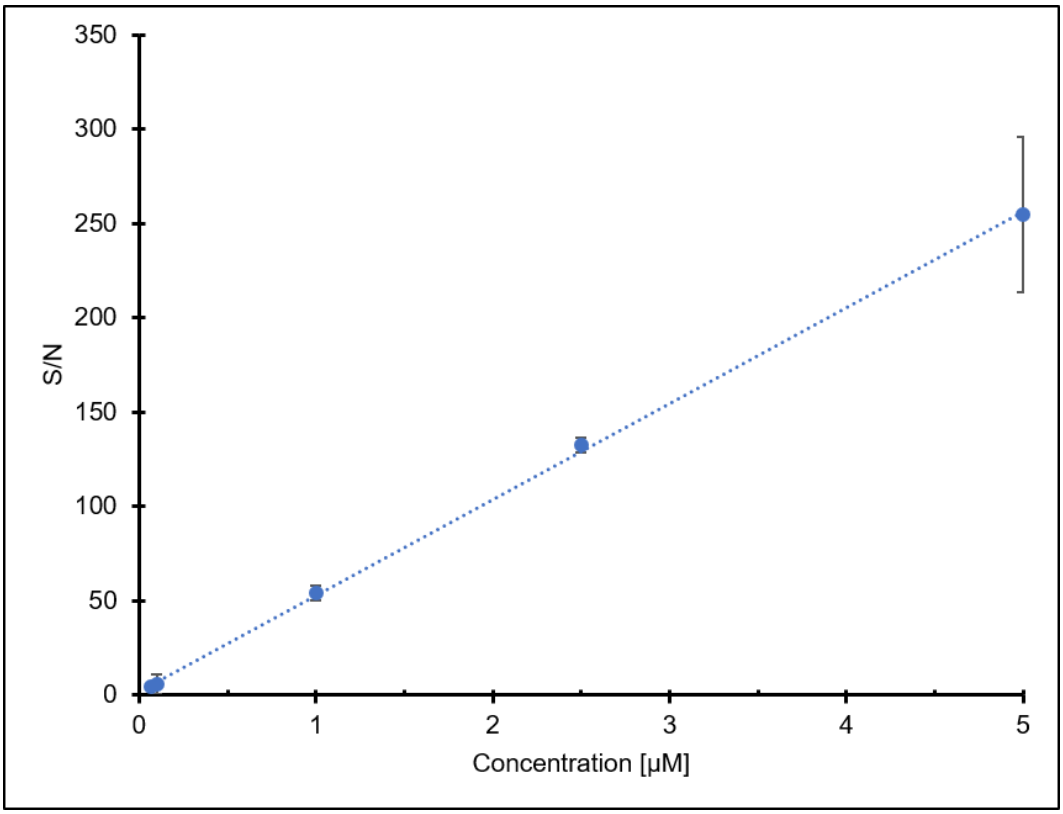
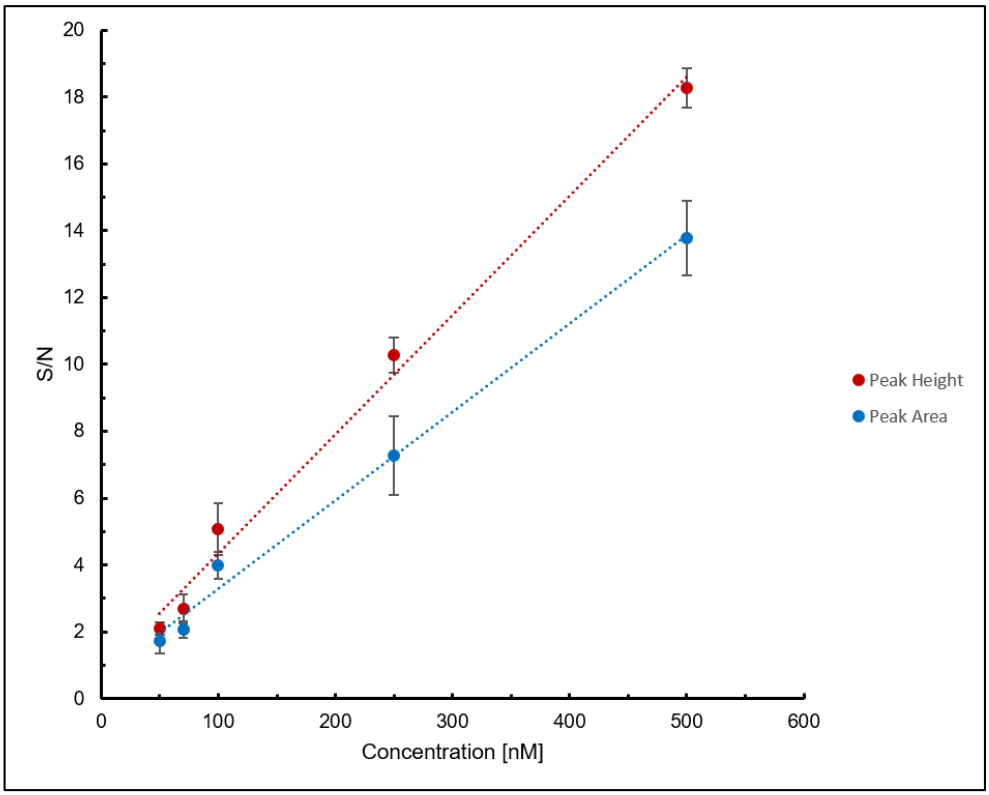


Figure 2.11: LOD of the system with dual polarizers and a reflector.

a.



b.

	LOD [nM]
Peak height	63±3.3
Peak area	89± 4.4

Figure 2.12: LOD of the system where the excitation source is modulated in which the S/N was determined for both peak height and peak area.

Chapter 3

3D Printed detectors for fluorescence polarization measurements

3.1 Introduction

The design of our detectors offer a wide variety applications that are beyond that of typical fluorescence detection. In previous work, we have successfully performed Taylor dispersion analysis (TDA) on fluorescein isothiocyanate (FITC) labeled amino acids[12]. This allowed us to perform size based measurements by measuring diffusion coefficients of molecules. With the addition of linear polarizers in our current detector build, fluorescence polarization measurements can be realized. As shown in equation 1.11, fluorescence polarization can be influenced by molecular size or by solvent viscosity, with the latter being a useful experimental parameter for modeling fluorescence polarization changes. Studies have shown that viscosity can also affect the quantum yield of a fluorophore by reducing the rate of relaxation processes and increasing its fluorescence lifetime.[39, 18]

In this work, we performed fluorescence polarization measurements as a proof of concept that it can be executed with our 3D printed detectors.

3.2 Material and methods

3.2.1 Reagents

Flouroscein disodium salt and sodium tetraborate were purchased from ThermoFisher Scientific (Waltham, MA). Borate buffer solution (10 mM) was prepared using water from Milli-Q purification system (Millipore, Bedford, MA) and pH adjusted to 8. Glycerol (56-81-5, Sigma-Aldrich, St. Louis, MO) and isopropanol (67-63-0, Fisher Scientific, Hampton, NH) were used to adjust viscosity of solution ranging from concentrations of 0-20 % . Fluorescein standards of 5 and 50 μM were prepared. Fresh solutions of buffer and standards were prepared each month.

3.2.2 Experimental setup

Assembly of the detector follow the same protocols as mentioned in 2.2.2. Due to minor uncontrolled variations in detector assemblies, sensitivity cannot be perfectly matched between multiple detectors, thus a single detector was used to collect polarized emission intensities of both parallel and perpendicular axes by rotating polarizers between successive measurements. The SevenCompact pH meter S220 (Mettler Toledo, Columbus, OH) was used to study pH effects of viscosity modifiers.

3.2.3 Polarization calculations

Polarization experiments were performed using pressure flow protocols similar to 2.2.3. To determine polarization values of fluoroscein in varying viscous solutions, the baseline subtracted signal of both parallel and perpendicular emissions were obtained, where one orientation could be observed for each experiment. Each point on the polarization plots were determined with n = 3 trials.

3.3 Results and discussion

3.3.1 Detection performance

Before proceeding to polarization experiments, the performance of each detector was observed to determine a viable concentration of fluoroscein to be used. In Figure 3.1, the observable noise from parallel detection was about seven times greater than perpendicular detection. Due to a lower amount of scatter rejection in the parallel mode, a much higher concentration of fluoroscein (50 μM) needed to be used for detection. Large disparity in LOD between both $\|+\|$ and $\|+\perp$ detection was also observed in the previous chapter in table 2.1.

3.3.2 pH dependence

The need for a more concentrated sample was also due to the environment of the fluorophore. While studies show that more viscous solutions increase quantum yield, the opposite effect was seen in this study.[9] Buffer modifiers can influence pH and in turn influence quantum yield of fluorescein. This study aimed to operate at a pH of 8, but it can be seen in table 3.1 that the addition of glycerol, which was added as a viscosity modifier, reduced the pH of the solution drastically. Fluorescein has two sites of protonation that can be influenced by pH to favor ionic structures ranging from dianionic to monocationic. This results in a shift of the absorption maxima, which is 437 nm for cations, 433 nm for neutral, 453 and 474 nm for anion, and 475 and 490 nm for dianion species.[35, 37] Because of the impact on fluorescence properties via pH effects, a lower concentration range of glycerol was used (0-20%). This effect was not seen to be nearly as detrimental in isopropanol solutions.

Table 3.1: pH dependence of quantum yield of fluorescein (5 μM)

Glycerol conc.	pH	S/N
0 %	8.14±0.02	107.61±12.08
10 %	5.69±0.01	39.47±4.05
15 %	5.05±0.01	6.10±0.94
20 %	4.56±0.01	3.81±0.65

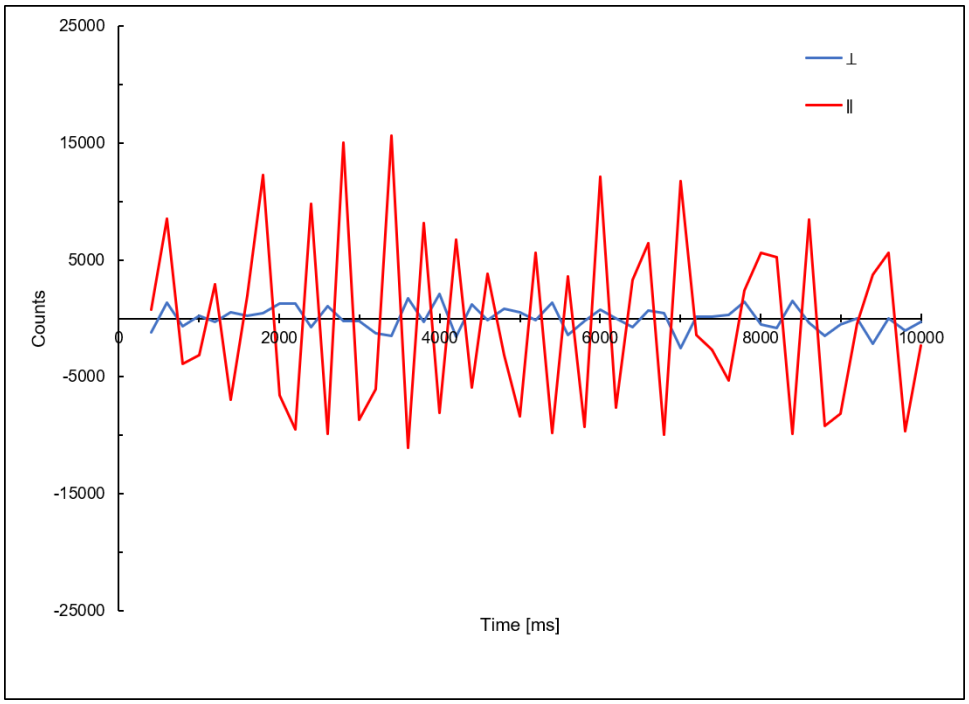


Figure 3.1: Baseline noise of both ∥ (red)and ⊥ (blue) collected signal for 10% glycerol solution.

3.3.3 Polarization experiments

As described in equation 1.11, polarization values are directly proportional to media viscosity. As viscosity increases, angular velocity of the fluorophore decreases so that polarization is increased and vice versa. Polarization values of glycerol and isopropanol solutions were calculated with equation 1.9 by using the baseline subtracted fluorescein signal intensities from both parallel and perpendicular detection. In Figure 3.2, polarization values of glycerol and isopropanol were shown to be highly negative with a decreasing trend towards higher glycerol and isopropanol content, which indicate that both solutions are highly depolarized. While the trend is expected when decreasing viscosity with isopropanol, it is unusual for glycerol, despite the opposite trend in literature.[18] The highly negative values were a result of a relatively low I_V value in comparison to I_H. Calculation error was no higher than 2%, indicating that the experiments were highly reproducible. We expect that the ratio-metric nature of polarization calculations should not be affected by the different signal intensities determined. Despite this, we hypothesize that the relatively high amount of noise introduced in the parallel mode lead to a discrepancy in the amount of light that was detected. By reducing the noise collected in the detection system, there could be a higher difference in signal intensity in the parallel mode similar to what is seen in the perpendicular mode. This would also help attenuate the highly negative polarization values. More work on improving scatter reduction will be discussed in the future directions of this detector.

3.4 Future directions

It is clear that light scatter from the capillary interface is a large detriment to fluorescence detection. The current band pass filters used for both excitation and emission have an optical density of 5 and 6 respectively. This allows a relatively small percentage of all light (>0.001 %) to be transmitted through both filters causing spectral overlap of emission with other light sources, meaning that the light detection is not limited purely to fluorescence. In order to achieve sub-nanomolar detection limits and improve fluorescence polarization quality, additional spectral rejection optics will be explored. It is common for a commercial spectrometer to use monochromators in addition to other spectral filters. The direction of

our work will focus on a ruled reflective diffraction grating due to the nature of its low cost fabrication method.

3.4.1 Reflection grating

Diffraction gratings are used to disperse polychromatic light into its component wavelengths. Reflection gratings are typically replicas produced from a master grating. Each grating has a particular groove profile where each groove or blaze is closely spaced and parallel with one another. Each groove face acts as a pseudo point source where interference interactions of light occur. The summation of these interferences display regions where a specified wavelength of light is at its maxima due to constructive interference and, regions where it is at its lowest due to destructive interference.[36] This relationship can be described by the following equation:

$$n\lambda = d(sini + sinr) \tag{3.1}$$

where n is a small whole number representing the diffracted order of light, d is the spacing between each groove, i is the angle of incidence, and r is the reflected angle where the intensity of λ is at a maxima. First order diffractions produce the highest intensity of light. The higher orders can be filtered with additional optics or can also be removed by modifying the angle of incidence.

The angle of separation of monochromatic light can be related to groove spacing and reflected angled of light if i is held constant. This is known as the angle of dispersion:

$$\frac{dr}{d\lambda} = \frac{n}{dcosr} \tag{3.2}$$

Effective spectral resolution also defines the distance and width of the slit needed to filter out multiple wavelengths. Linear dispersion is another useful metric that can be used to define appropriately sized slits. Linear dispersion is the width of the image per unit wavelength defined by the equation:

$$D = \frac{dy}{d\lambda} = f\frac{dr}{d\lambda} \tag{3.3}$$

where f is the focal distance between the monochromator and focal plane of the slit.

3.4.2 Future designs

To reduce spectral overlap of excitation and emission, several designs have been proposed implementing the monochromator (GR13-1850, Thorlabs Inc. Newton, NJ). Here in Figure 3.3 the original detector design is modified to incorporate a diffraction grating in the emission axis to allow spectral filtration of both excitation and emission light. Emission collected by the ball lens is collimated through a pinhole, where a polarization filter perpendicular to the groove direction will precede the grating to maximize the diffraction efficiency. This placement will also allow the detector to retain its polarization measurement functionality. With a blaze rating of 1800/mm, the angle of incidence of emission was determined to be 15.1°. This angle provides many advantages including: displaying the highest range of angles in the visible spectrum while also maximizing their angular dispersion and eliminating the majority of light produced after the first order. At this angle, 490 nm light is diffracted at 38.4° while 525 nm is diffracted at 43.2°. Emission is filtered by a small slit or pinhole placed in the angular direction of the emitting light.

Spectral resolution is limited to the spatial resolution provided by 3D printing. Both FDM and SLA formats have been explored previously to determine the smallest achievable pinhole size (0.81 and 0.4 mm respectively) as shown in Figure 3.4 . So optimization of the focal length will be influenced accordingly.

Figure 3.5 showcases a confocal based design, should it be revisited again. By removing the pinhole preceding the polarization filter, a higher intensity of emission may be preserved and focused through a pinhole while rejecting out of focus scatter.

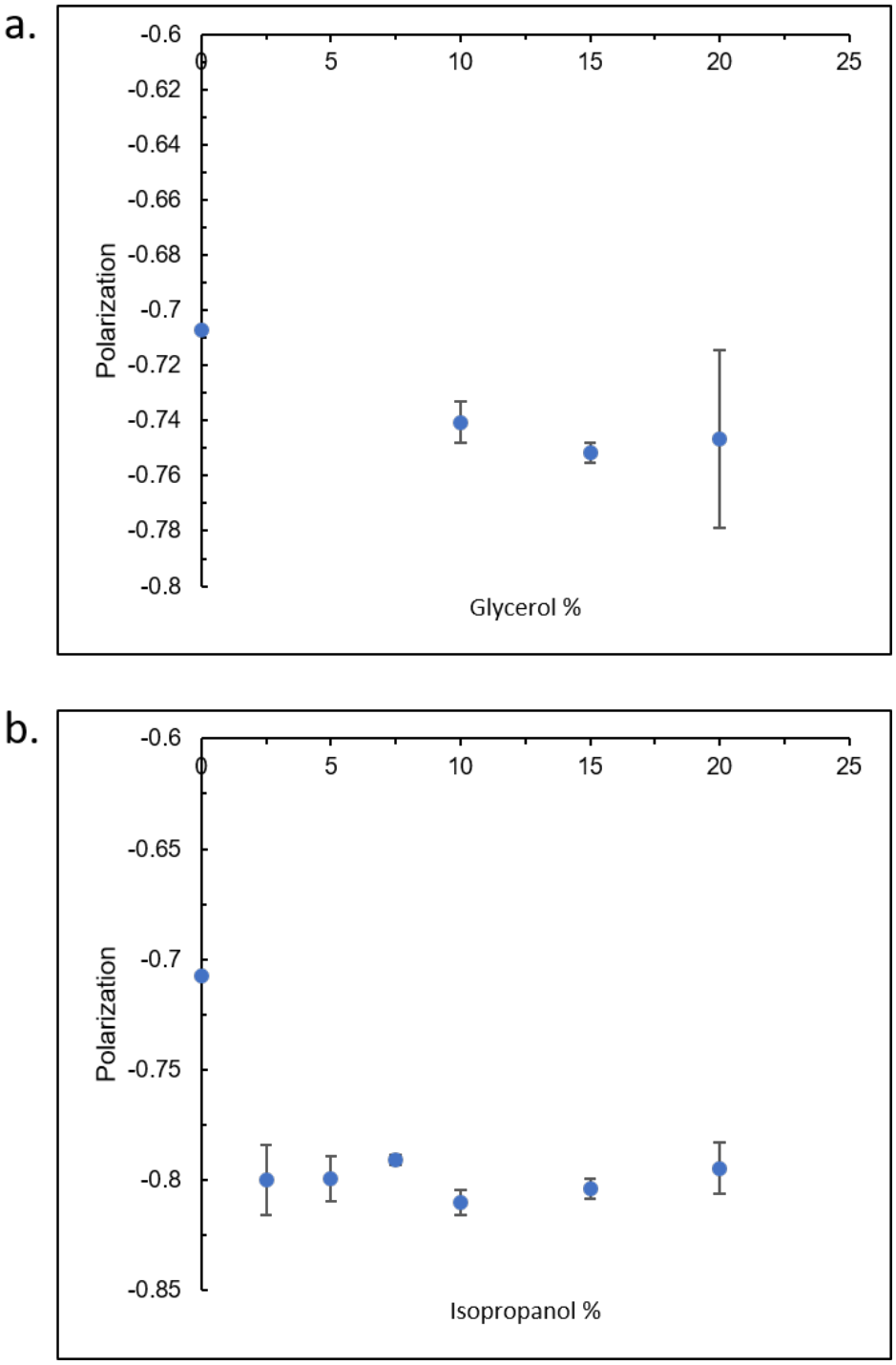


Figure 3.2: Polarization values of a) glycerol and b) isopropanol solutions

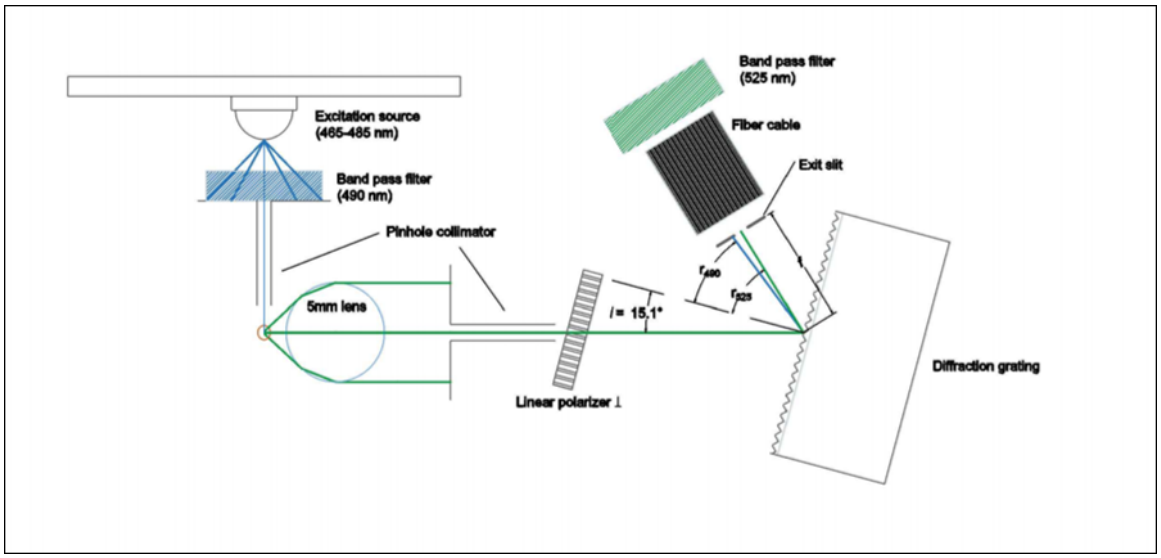


Figure 3.3: Schematic of future monochromator based detector.

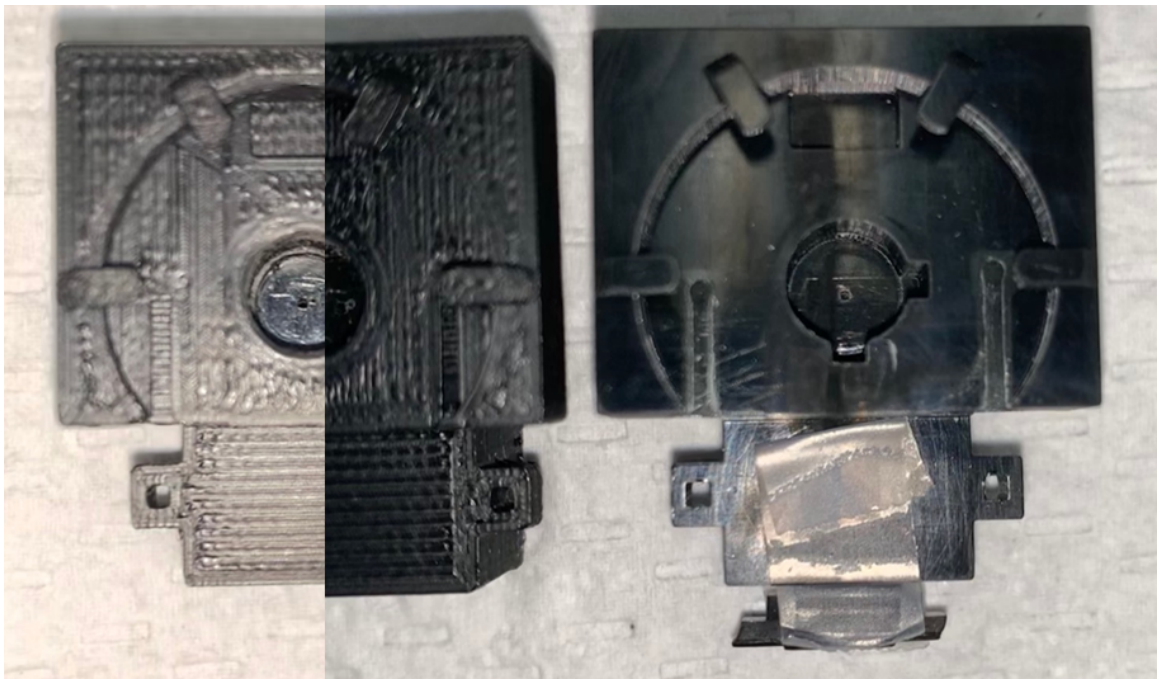


Figure 3.4: Varying achievable pinhole sizes of FDM (left) 0.81 mm and SLA (right) at 0.4 mm.

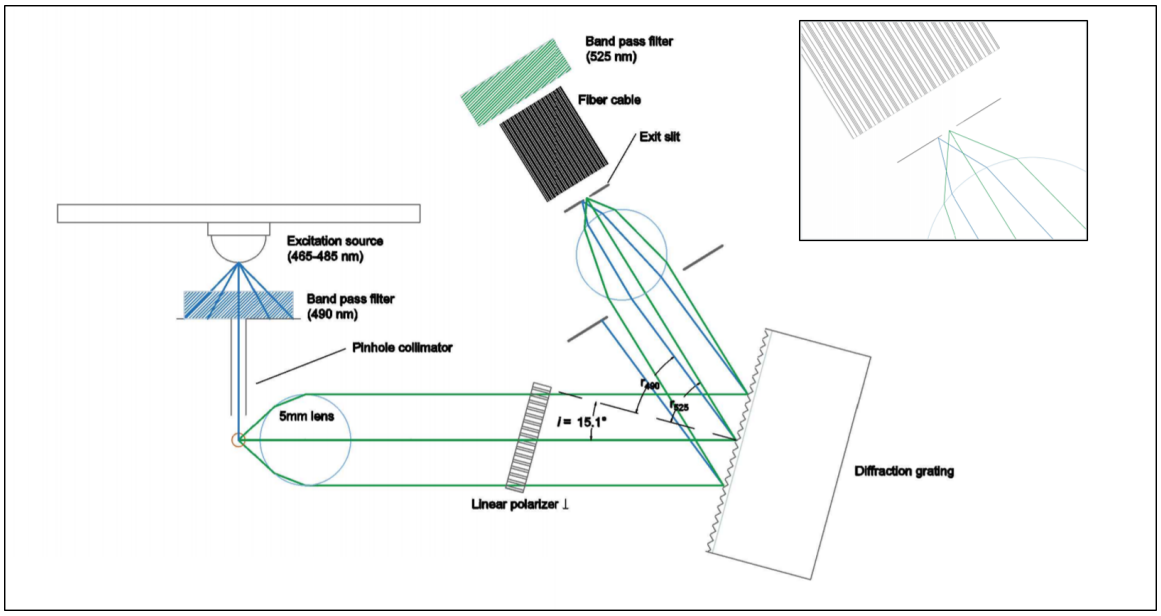


Figure 3.5: Second variation of monochromator detector design incorporating a focusing lens.

3.5 Conclusion

This study illustrates an application of our 3D printed detector. The main benefit of linear polarizers was to increase rejection of scatter, and the ability to perform fluorescence polarization measurements were auxiliary to this. Altering the viscosity environment of fluoroscein allowed for several polarization measurements to be obtained. Both glycerol and isopropanol solutions show high depolarization values with a decreasing trend. This and worsened LOD conditions are likely to be limited by poor detection performance in the parallel orientation. With this in mind, scatter rejection quality can be improved by increasing spectral resolution between excitation and emission. We plan in improving spectral resolution by incorporating a diffraction grating along the emission axis. We believe that 3D printing will be key to aiding the complexity of this design.

Bibliography

[1] (1984). Apparatus for production of three-dimensional objects by stereolithography. 8

[2] (1989). Apparatus and method for creating three-dimensional objects. 8

[3] (2016). *The Analysis of Time Series*. Chapman and Hall/CRC. 3

[4] Alessandri, K., Feyeux, M., Gurchenkov, B., Delgado, C., Trushko, A., Krause, K.-H., Vignjević, D., Nassoy, P., and Roux, A. (2016). A 3D printed microfluidic device for production of functionalized hydrogel microcapsules for culture and differentiation of human Neuronal Stem Cells (hNSC). *Lab on a Chip*, 16(9):1593–1604. 8

[5] Allen, P. B., Doepker, B. R., and Chiu, D. T. (2007). Fourier transform capillary electrophoresis with laminar-flow gated pressure injection. *Analytical Chemistry*. 4

[6] Attia, U. M., Marson, S., and Alcock, J. R. (2009). Micro-injection moulding of polymer microfluidic devices. *Microfluidics and Nanofluidics*, 7(1):1–28. 8

[7] Au, A. K., Huynh, W., Horowitz, L. F., and Folch, A. (2016). 3D-Printed Microfluidics. *Angewandte Chemie International Edition*, 55(12):3862–3881. 8

[8] Becker, H. and Locascio, L. E. (2002). Polymer microfluidic devices. *Talanta*, 56(2):267–287. 8

[9] Berezin, M. Y. and Achilefu, S. (2010). Fluorescence lifetime measurements and biological imaging. *Chemical Reviews*. 7, 33

[10] Bertsch, A., Heimgartner, S., Cousseau, P., and Renaud, P. (2001). Static micromixers based on large-scale industrial mixer geometry. *Lab on a Chip*, 1(1):56. 8

[11] Bjorklund, G. C. (1980). Frequency-modulation spectroscopy: a new method for measuring weak absorptions and dispersions. *Optics Letters*. 7

[12] Casto, L., Do, K. B., and Baker, C. A. (2019). A miniature 3D printed LED-induced fluorescence detector for capillary electrophoresis and dual detector Taylor dispersion analysis. *Analytical chemistry*. 10, 11, 12, 31

[13] Chen, C. S., Chen, W. N., Zhou, M., Arttamangkul, S., and Haugland, R. P. (2000). Probing the cathepsin D using a BODIPY FL-pepstatin A: applications in fluorescence polarization and microscopy. *Journal of biochemical and biophysical methods*, 42(3):137–51. 7

[14] Chen, D. Y. and Dovichi, N. J. (1994). Yoctomole detection limit by laser-induced fluorescence in capillary electrophoresis. *Journal of chromatography. B, Biomedical applications*, 657(2):265–9. 5

[15] Cleemann, F. and Karuso, P. (2008). Fluorescence Anisotropy Assay for the Traceless Kinetic Analysis of Protein Digestion. *Analytical Chemistry*, 80(11):4170–4174. 7

[16] Crabtree, H. J. (1999). Shah convolution fourier transform detection. *Analytical Chemistry*. 4

[17] David Heiger (2000). *An introduction: High performance capillary electrophoresis*. Agilent Technologies. 2

[18] Fixler, D., Namer, Y., Yishay, Y., and Deutsch, M. (2006). Influence of Fluorescence Anisotropy on Fluorescence Intensity and Lifetime Measurement: Theory, Simulations and Experiments. *IEEE Transactions on Biomedical Engineering*, 53(6):1141–1152. 31, 35

[19] Flecha, F. L. G. and Levi, V. (2003). Determination of the molecular size of BSA by fluorescence anisotropy. *Biochemistry and Molecular Biology Education*. 7

[20] German, I. and Kennedy, R. T. (2000). Rapid simultaneous determination of glucagon and insulin by capillary electrophoresis immunoassays. *Journal of Chromatography B: Biomedical Sciences and Applications*, 742(2):353–362. 5

[21] Gross, B., Lockwood, S. Y., and Spence, D. M. (2017). Recent Advances in Analytical Chemistry by 3D Printing. *Analytical Chemistry*, 89(1):57–70. 1, 8

[22] Guillo, C. and Roper, M. G. (2008). Two-color electrophoretic immunoassay for simultaneous measurement of insulin and glucagon content in islets of Langerhans. *ELECTROPHORESIS*, 29(2):410–416. 5

[23] Guillo, C. and Roper, M. G. (2011). Simultaneous capillary electrophoresis competitive immunoassay for insulin, glucagon, and islet amyloid polypeptide secretion from mouse islets of Langerhans. *Journal of Chromatography A*, 1218(26):4059–4064. 5

[24] Hwang, Y., Paydar, O. H., and Candler, R. N. (2015). 3D printed molds for non-planar PDMS microfluidic channels. *Sensors and Actuators A: Physical*, 226:137–142. 8

[25] Jameson, D. M. and Ross, J. A. (2010). Fluorescence polarization/anisotropy in diagnostics and imaging. *Chemical reviews*, 110(5):2685–708. 6

[26] Kobayashi, S., Yamamoto, Y., Ito, M., and Kimura, T. (2004). Direct frequency modulation in AlGaAs semiconductor lasers. *IEEE Journal of Quantum Electronics*. 7

[27] Lomasney, A. R., Yi, L., and Roper, M. G. (2013). Simultaneous Monitoring of Insulin and Islet Amyloid Polypeptide Secretion from Islets of Langerhans on a Microfluidic Device. *Analytical Chemistry*, 85(16):7919–7925. 5

[28] Mesbah, K., Verpillot, R., Chiari, M., Pallandre, A., and Taverna, M. (2014). Neutral polymers as coatings for high resolution electrophoretic separation of A peptides on glass microchips. *Analyst*. 1

[29] Nie, K., Stickney, G., and Zeng, F. G. (2005). Encoding frequency modulation to improve cochlear implant performance in noise. *IEEE Transactions on Biomedical Engineering*. 7

[30] Nielsen, R. G., Rickard, E. C., Santa, P. F., Sharknas, D. A., and Sittampalam, G. S. (1991). Separation of antibody-antigen complexes by capillary zone electrophoresis, isoelectric focusing and high-performance size-exclusion chromatography. *Journal of chromatography*, 539(1):177–85. 4

[31] Patrick, W. G., Nielsen, A. A. K., Keating, S. J., Levy, T. J., Wang, C.-W., Rivera, J. J., Mondragón-Palomino, O., Carr, P. A., Voigt, C. A., Oxman, N., and Kong, D. S. (2015). DNA Assembly in 3D Printed Fluidics. *PloS one*, 10(12):e0143636. 8

[32] Phillips, T. M. and Wellner, E. F. (2007). Analysis of inflammatory biomarkers from tissue biopsies by chip-based immunoaffinity CE. *ELECTROPHORESIS*, 28(17):3041–3048. 5

[33] Prikryl, J. and Foret, F. (2014). Fluorescence Detector for Capillary Separations Fabricated by 3D Printing. *Analytical Chemistry*, 86(24):11951–11956. 8

[34] Rodat-Boutonnet, A., Naccache, P., Morin, A., Fabre, J., Feurer, B., and Couderc, F. (2012). A comparative study of LED-induced fluorescence and laser-induced fluorescence in SDS-CGE: Application to the analysis of antibodies. *ELECTROPHORESIS*, 33(12):1709–1714. 10

[35] Sjöback, R., Nygren, J., and Kubista, M. (1995). Absorption and fluorescence properties of fluorescein. *Spectrochimica Acta Part A: Molecular Spectroscopy*. 33

[36] Skoog, D. A. and Leary, J. J. (1992). *Principles of instrumental analysis*. Saunders College Pub. 36

[37] Slyusareva, E. A., Gerasimov, M. A., Sizykh, A. G., and Gornostaev, L. M. (2011). Spectral and fluorescent indication of the acid-base properties of biopolymer solutions. *Russian Physics Journal*, 54(4):485–492. 33

[38] Su, C.-K., Yen, S.-C., Li, T.-W., and Sun, Y.-C. (2016). Enzyme-Immobilized 3D-Printed Reactors for Online Monitoring of Rat Brain Extracellular Glucose and Lactate. *Analytical Chemistry*, 88(12):6265–6273. 8

[39] Turgeman, L. and Fixler, D. (2013). Time-averaged fluorescence intensity analysis in fluorescence fluctuation polarization sensitive experiments. *Biomedical optics express*, 4(6):868–84. 31

Appendices

A Additional schematics

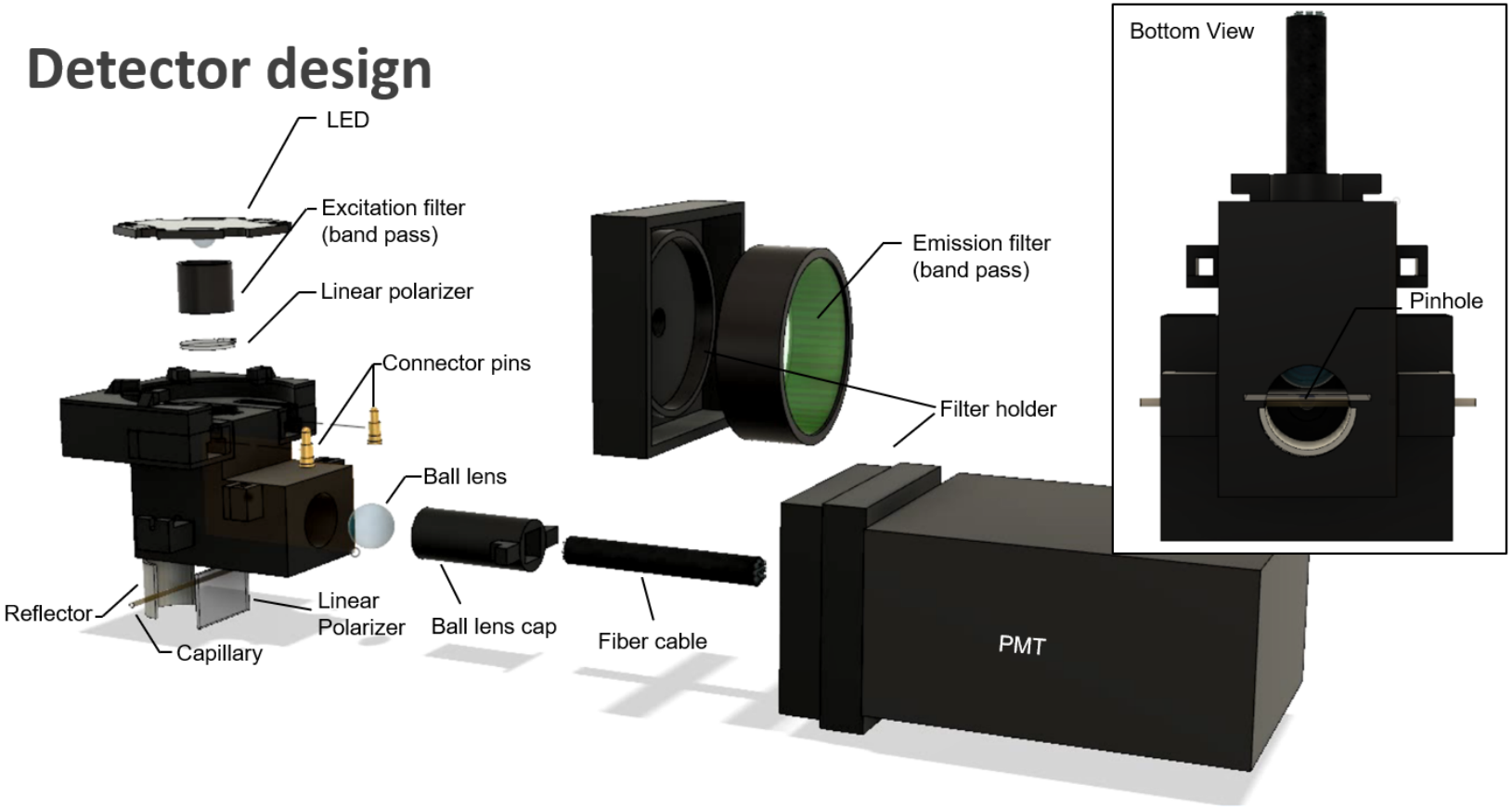


Figure A.1: Detector schematic (current build).

Vita

Kevin Do, born in a local hospital in West Covina, California, is a boy that grew up moving around all over the country living in big cities his whole life. Each location change made it more difficult for him to settle down into a place he could call home. And despite this, the one thing that remained constant in his life was the sound of the hustling and bustling cities that he resided in, and this gave him comfort. He attended college at Arizona State University where he explored his curiosity for science. He earned his B.S. degree in chemistry, May of 2016. His interests are ever-changing and he is almost always excited to try new things. Looking for a change of pace and experiencing a different culture from his own, he moved to Knoxville, Tennessee where he joined a graduate program at the University of Tennessee, Knoxville. There he would pursue an interest in engineering applications within the chemical field, a side of himself he never saw. Eager to flex his creative muscles, Kevin approached each project with excitement, seeing what he could design next. His creativity is an extension of his personal life and can be seen by his love for playing music and drawing in his spare time. He will earn his M.S. in analytical chemistry in Fall 2019. After, he will plan his next big move and try to discover where home is meant to be. Although, home may be closer to him than what he thinks.